Received: 3 April 2019 | Revised: 16 July 2019 | Accepted: 9 September 2019 | Published on: 11 October 2019

DOI: 10.1002/qj.3660

RESEARCH ARTICLE

Quarterly Journal of the Royal Meteorological Society RMetS

Changes in mean flow and atmospheric wave activity in the North Atlantic sector

Heiko Paeth | Felix Pollinger

Institute of Geography and Geology, University of Würzburg, Würzburg, Germany

Correspondence
Heiko Paeth, Institute of Geography and Geology, University of Würzburg, Am Hubland, 97070 Würzburg, Germany.
Email: heiko.paeth@uni-wuerzburg.de

Abstract

In recent years, the midlatitudes are characterized by more intense heatwaves in summer and sometimes severe cold spells in winter that might emanate from changes in atmospheric circulation, including synoptic-scale and planetary wave activity in the midlatitudes. In this study, we investigate the heat and momentum exchange between the mean flow and atmospheric waves in the North Atlantic sector and adjacent continents by means of the physically consistent Eliassen–Palm flux diagnostics applied to reanalysis and forced climate model data. In the long-term mean, momentum is transferred from the mean flow to atmospheric waves in the northwest Atlantic region, where cyclogenesis prevails. Further downstream over Europe, eddy fluxes return momentum to the mean flow, sustaining the jet stream against friction. A global climate model is able to reproduce this pattern with high accuracy. Atmospheric variability related to atmospheric wave activity is much more expressed at the intraseasonal rather than the interannual time-scale. Over the last 40 years, reanalyses reveal a northward shift of the jet stream and a weakening of intraseasonal weather variability related to synoptic-scale and planetary wave activity. This pertains to the winter and summer seasons, especially over central Europe, and correlates with changes in the North Atlantic Oscillation as well as regional temperature and precipitation. A very similar phenomenon is found in a climate model simulation with business-as-usual scenario, suggesting an anthropogenic trigger in the weakening of intraseasonal weather variability in the midlatitudes.

KEYWORDS

atmospheric waves, climate change, Eliassen–Palm flux, jet stream

1 | INTRODUCTION

Human activity is supposed to have manifold implications for the Earth's climate system (IPCC, 2013). Concerning spatio-temporal patterns of transient temperature changes all around the globe and directly associated phenomena such as increasing heat days, decreasing frost days and snow cover, we have a well-grounded process understanding of their relationship with radiative forcing and can assign a large portion of recent trends to man-made climate change (e.g. IPCC, 2013; Shepherd, 2014). Other weather and climate characteristics that occurred more intensely or more frequently in recent decades emanate from a more complex process chain, potentially initiated by greenhouse warming as

This is an open access article under the terms of the Creative Commons Attribution License, which permits use, distribution and reproduction in any medium, provided the original work is properly cited.
© 2019 The Authors. *Quarterly Journal of the Royal Meteorological Society* published by John Wiley & Sons Ltd on behalf of the Royal Meteorological Society.

well. Prominent examples are the severe heatwaves and cold spells observed since the turn of the millennium in various midlatitude regions (e.g. Cohen *et al.*, 2014; Horton *et al.*, 2015; Petoukhov *et al.*, 2018), a tendency that is corroborated by global climate change projections until the end of the twenty-first century (Russo *et al.*, 2014). While heatwaves may be intuitively associated with global warming, cold spells often lead to some uncertainty about the evidence of anthropogenic climate change in the public and require plausible scientific explanations. This implies a thorough look at how atmospheric dynamics may respond to radiative forcing. These mechanisms are much less understood because atmospheric circulation is a paradigm for the chaotic nonlinear nature and internal variability of the climate system (Shepherd, 2014; Barnes and Screen, 2015; Overland *et al.*, 2016).

In recent years, a theory has been developed linking changes in weather variability and extremes in the midlatitudes to the big picture of a warming planet. The main trigger is the spatially differentiated warming pattern with the polar caps denoting temperature increases twice as much as on global average, especially in the Arctic (IPCC, 2013; Cohen *et al.*, 2014). This phenomenon mainly arises from decreasing sea ice and snow cover extent, including the ice-albedo feedback, and is referred to as the Arctic amplification (Coumou *et al.*, 2018). Consequently, the meridional temperature gradient is weakening (Mann *et al.*, 2017) and, according to the thermal wind balance, the westerly jet stream reduces in strength and shifts equatorward (Dethloff, 2006; Perlwitz *et al.*, 2015; Molnos *et al.*, 2017). This in turn affects the activity of planetary waves and extratropical cyclones, involving a negative phase of the North Atlantic Oscillation (NAO) and Northern Annular Mode (NAM) and stimulating a feedback of the stratospheric polar vortex that tends to elongate the circulation anomaly in time (Kim *et al.*, 2014; Vihma, 2014; Jaiser *et al.*, 2016). The process finally results in more persistent planetary wave configurations, large-scale circulation patterns and regional weather types in the midlatitudes that produce weather extremes of all types, e.g. dry and hot, cold and dry, or extremely wet with rainfall or snow (Dethloff, 2006; Handorf *et al.*, 2015; Perlwitz *et al.*, 2015; Petoukhov *et al.*, 2018).

While this mechanism is most active in Northern Hemisphere winter (Shepherd, 2016), several authors have also identified a clear tendency towards more persistent heatwaves in summer, especially over Northern Hemisphere land masses (Horton *et al.*, 2015; Kornhuber *et al.*, 2017; Coumou *et al.*, 2018; Hoffmann, 2018; Pfleiderer and Coumou, 2018). Mann *et al.* (2017) have shown that midlatitude atmospheric waves with synoptic-scale wave numbers are more frequently trapped in so-called waveguides that prevail during the summer season and cause longer phases with the same weather conditions in a given region. Yet, other authors have pointed to changes in the upper tropical atmosphere which, towards the late twenty-first century, may dominate over the Arctic amplification in triggering circulation changes in the midlatitudes (Barnes and Screen, 2015). Thus, processes may be more complicated and are, hence, still subject to a vivid scientific debate.

In the present study, we contribute to this debate by investigating the physical link between changes in the zonal mean flow and atmospheric wave activity in the North Atlantic sector, including western Europe and eastern North America. This region is focused on for several reasons: (a) the North Atlantic is a source region for planetary waves because a quasi-stationary wave pattern is established downstream of the frictional effect of the North American continent and the Rocky Mountains (Shimizu and de Albuquerque Cavalcanti, 2011), (b) the adjacent continents have been severely affected by recent heatwaves and cold spells (Horton *et al.*, 2015), (c) air traffic peaks over the North Atlantic and is very sensitive to changes in the jet stream strength and position, and (d) the density of meteorological ground and radiosonde stations is among the highest worldwide giving more confidence in the upper-tropospheric reanalysis data used here (Dee *et al.*, 2011).

The waviness of the midlatitude atmospheric flow and the interactions with the mean flow are diagnosed based on a sophisticated physically consistent metric, the Eliassen–Palm flux (EPF) approach, that is derived from the set of thermodynamic primitive equations and satisfies the laws of mass conservation and budget closure (Trenberth, 1986). The EPF diagnostics are dedicated to an improved process understanding of atmospheric dynamics at the scale of midlatitude eddies and avoids typical problems of geometric and Fourier-based assessments of waviness such as artificial wave signals and averaging effects (cf. Nakamura and Zhu, 2010; Huang and Nakamura, 2016; Coumou *et al.*, 2018). Originally, it has been used to study weather phenomena at the synoptic time-scale such as individual blocking events (e.g. Trenberth, 1986). Recently, it has also been applied to the context of the Arctic amplification (Handorf *et al.*, 2015; Jaiser *et al.*, 2016). Recently, Nakamura and Solomon (2010; 2011) have presented the finite-amplitude wave activity framework that is close to the EPF approach but tends to improve the signal-to-noise ratio for climatological applications.

Here, we aim at a statistical assessment of the EPF diagnostics applied to reanalysis and climate model data. There are five main objectives underlying the study design: (a) the mean characteristics of the interactions between mean flow and atmospheric waves will be elucidated, including the weather and climate variability that arises from wave activity in the Atlantic sector, (b) the total wave activity is differentiated between synoptic-scale and planetary waves in order to gain insight into the specific behaviour of extratropical cyclones and Rossby waves (cf. Di Biagio *et al.*, 2014), (c) a

major focus is on observed changes in intraseasonal weather variability related to trends of the zonal mean flow and the associated response of eddy fluxes in the midlatitudes, (d) these changes are linked to large-scale circulation indices and regional climate anomalies to evaluate the climatological interpretability of the metric, and (e) the EPF diagnostics are applied to climate model data to assess whether anthropogenic climate forcing may affect midlatitude atmospheric circulation and weather variability.

Our analysis refers to three scientific hypotheses: (a) recently observed changes in upper-tropospheric wave activity and weather variability over the North Atlantic sector can be illustrated by means of the EPF diagnostics, (b) a coarser-grid global climate model simulates similar patterns of upper-tropospheric mean circulation, interannual and intraseasonal variability and eddy forcing as found in reanalyses, and (c) atmospheric wave activity in the North Atlantic sector is sensitive to radiative heating implemented in a global climate model simulation.

The following section provides insight into the considered reanalysis and climate model data and the methodology including the EPF diagnostics. Section 3 is dedicated to the results, subdivided into three subsections addressing the climatological characteristics in the ERA-Interim reanalysis, the observed changes and the simulated changes until the end of the twenty-first century. Section 4 discusses the results in the light of the existing literature and draws the main conclusions with respect to the hypotheses mentioned above.

2 | METHODS AND DATA

The EPF diagnostics have been developed by Eliassen and Palm (1961) with the aim of describing the energy transfer in orographically induced stationary waves. Here, we apply the localized approach suggested by Trenberth (1986) that allows for a grid box-wise computation on an atmospheric pressure level. The basic equations dealt with in this study describe the momentum equations for the mean zonal ($\overline{u}$) and meridional ($\overline{v}$) wind components in a given grid box, formulated in spherical geometry with a vertical pressure coordinate. They refer to the set of primitive equations, i.e. prognostic equations for momentum, mass and heat (Szunyogh, 2015), and split the values of all considered variables x up into the mean $\overline{x}$ and the anomalies x'. Here, we use temporal means over a season, marked by an overbar in the following equations. The approach emanates from a number of assumptions and approximations to reach a pair of solvable and manageable equations that satisfy the continuity equation: (a) quasi-geostrophic approximation, i.e. no vertical motion ($\overline{\omega} = 0$) and no frictional processes ($F_{x,y,z} = 0$), (b) hydrostatic approximation ($\nabla_{\mathrm{H}}\rho = 0$), and (c) constant density ($\rho' = 0$). Using the horizontal wind components u and v, temperature T, potential temperature θ, geopotential Φ, density ρ, Coriolis parameter $f = 2\Omega\sin\varphi$, geographical coordinates λ and φ, Earth's radius r_{E}, and specific gas constant R_{L}, the resulting pair of basic equations is listed and explained below. For a more detailed description and derivation refer to Trenberth (1986):

$$\frac{\partial \overline{u}\cos\varphi}{\partial t} - \frac{\overline{uv}\sin\varphi}{r_E} - f v^*\cos\varphi = -\overline{\mathbf{v}_{\mathrm{H}}}\nabla_{\mathrm{H}}\overline{u}\cos\varphi + \nabla_{\mathrm{E}}\overline{\mathbf{E}_u} + R_x, \tag{1}$$

$$\underbrace{\frac{\partial \overline{v}\cos\varphi}{\partial t}}_{I} + \underbrace{\frac{\overline{u}^2\sin\varphi}{r_E}}_{II} + \underbrace{f u^*\cos\varphi}_{III} = \underbrace{-\overline{\mathbf{v}_{\mathrm{H}}}\nabla_{\mathrm{H}}\overline{v}\cos\varphi}_{IV} + \underbrace{\nabla_{\mathrm{E}}\overline{\mathbf{E}_v}}_{V} + \underbrace{R_y}_{VI}. \tag{2}$$

u^* and v^* represent the components of the horizontal residual circulation that remains when the geostrophic and hydrostatic balances are reached:

$$u^* = \overline{u} + \frac{1}{f}\frac{\partial(\overline{\Phi}+\overline{K})}{\partial y} - \frac{1}{\rho}\frac{\partial}{\partial z}\left(\rho\frac{\overline{u'\Phi'_z}}{S}\right), \tag{3}$$

$$v^* = \overline{v} - \frac{1}{f}\frac{\partial(\overline{\Phi}+\overline{K})}{\partial x} - \frac{1}{\rho}\frac{\partial}{\partial z}\left(\rho\frac{\overline{v'\Phi'_z}}{S}\right), \tag{4}$$

with the kinetic energy contributed by the anomalous horizontal wind components

$$\overline{K} = \frac{1}{2}(\overline{u'^2} + \overline{v'^2}), \tag{5}$$

the static stability

$$S = \left(\frac{\partial\overline{\Phi_z}}{\partial z} - \frac{d\overline{\Phi_z}}{dz}\right) = \frac{\overline{\Phi_z}}{\theta}\frac{\partial\theta}{\partial z}, \tag{6}$$

and the mass-specific energy for expansion work

$$\overline{\Phi_z} = R_{\mathrm{L}}\overline{T}. \tag{7}$$

The EPF vectors are given by

$$\overline{\mathbf{E}_u} = \left[\frac{1}{2}(\overline{v'^2} - \overline{u'^2}), -\overline{u'v'}, f\frac{\overline{v'\Phi'_z}}{S}\right]^{\mathrm{T}}\cos\varphi, \tag{8}$$

$$\overline{\mathbf{E}_v} = \left[-\overline{u'v'}, -\frac{1}{2}(\overline{v'^2} - \overline{u'^2}), -f\frac{\overline{u'\Phi'_z}}{S}\right]^{\mathrm{T}}\cos\varphi, \tag{9}$$

with the mass-conserving divergence operator

$$\nabla_{\mathrm{E}} = \left[\frac{1}{r_{\mathrm{E}} \cos\varphi} \frac{\partial}{\partial \lambda} \;,\; \frac{1}{r_{\mathrm{E}}} \frac{1}{\cos\varphi} \frac{\partial}{\partial \varphi} \cos\varphi \;,\; \frac{1}{\rho} \frac{\partial}{\partial z} \rho \right]^{\mathrm{T}} \quad (10)$$

The exponent "T" denotes the transpose of the given column vectors.

The momentum equations comprise six terms. On the left-hand side, these are the local time derivatives of the horizontal wind components (I), the geometric terms arising from spherical coordinates (II), and the residual circulation described above (III). Together, they are representative of the localized atmospheric flow. On the right-hand side, the equations are composed of the advection term related to the mean flow (IV), the eddy forcing term as the major remaining source term of momentum (V), and the residuum (VI) that summarizes all processes disregarded due to the approximations. These are frictional processes, processes related to vertical motion, and sub-scale effects such as micro-turbulence in the atmospheric boundary layer. In the case of stationarity $\left(\frac{\partial}{\partial t} = 0\right)$, terms (II) to (V) can be computed from a given set of atmospheric variables, implying that the residuum can also be sized as a measure of how dominantly the atmospheric horizontal mean flow is governed by the eddy source term (V).

The EPF vectors in Equations 8 and 9 are three-dimensional with turbulent fluxes of momentum by eddies in the horizontal components and turbulent heat fluxes by eddies in the vertical component. The x- and y-components represent the barotropic part, the y- and z-components are combined to the baroclinic part, accounting for temperature gradients on a pressure level. The divergence of the EPF vectors indicates the genesis and formation of wave perturbations and their interaction with the zonal ($\overline{\mathbf{E}_u}$) and meridional ($\overline{\mathbf{E}_v}$) mean flow. A negative value, i.e. convergence of the EPF vector, means that heat and momentum is transferred from the mean flow to atmospheric waves, slowing down the mean flow. This occurs in areas where orographic forcing of Rossby waves and cyclogenesis take place. Where the EPF is divergent, wave perturbations dissipate and return heat and momentum to the mean flow, sustaining the latter against friction. This typically happens further downstream of the areas mentioned above.

To learn more about the specific processes related to eddies at the synoptic scale (extratropical lows and highs) and at the planetary scale (Rossby waves), the total day-to-day variability is bandpass filtered using 2–6 days for synoptic-scale perturbations and 10–90 days for planetary waves. This distinction has also been made by other authors (e.g. Di Biagio *et al.*, 2014). Note that with the use of daily-mean data, micro-turbulence over a time-scale of minutes to hours is not taken into account. This effect is subsumed under the residuum term (VI) in Equations 1 and 2. The bandpass filter uses binomial filter weights, i.e. the numbers from Pascal's triangle scaled to the sum of one. E.g. for a bandpass filter of 2–6 days, the time series at every grid box are first low-pass filtered over 2 days and over 6 days separately. Then, the 2-day low-pass filtered time series is subtracted from the 6-day low-pass filtered time series and the time series' mean is added to keep the original unit and co-domain. Using binomial filter weights retains more of the amplitudes of daily weather variability than an unweighted running-mean filter (cf. Blackmon, 1976; Wilks, 2006). For the statistical assessment of EPF diagnostics, we use standard statistics such as the t-test for estimating the significance of correlation coefficients and linear changes (linear trend multiplied by number of time steps).

The computation of the EPF diagnostics requires grids of temperature, horizontal wind velocity and geopotential height. All other variables in Equations 1–10 can be derived from this set of output variables. Due to the vertical derivatives in Equations 3, 4 and 10, the data must be available at several pressure levels. Here, we rely on the European Centre for Medium-Range Weather Forecasts ERA-Interim reanalyses in 0.75° resolution over the period 1979–2018 (Dee *et al.*, 2011). For the reasons given in section 1, the study is focused on the North Atlantic sector with adjacent land masses, covering the domain 90°W–30°E and 20°N–85°N (see domain in Figure 2). Atmospheric wave activity peaks in winter (Shepherd, 2016), but we are also interested in summertime dynamics and changes because they may relate to heat waves and flooding events in the midlatitudes (e.g. Pfleiderer and Coumou, 2018). Therefore, the 300 hPa level (∼9,000 m a.s.l.) has been chosen as the reference level for upper-tropospheric flow because it is located all-season under the tropopause, exhibiting a continuous meridional temperature gradient from the Pole to the Tropics (Szunyogh, 2015). In addition, this upper-tropospheric level meets some of the underlying assumptions, i.e. the quasi-geostrophic approximation and barely any vertical motion under the tropopause (see above). For this reason, the EPF diagnostics are not applied to lower- or mid-tropospheric levels where vertical motion peaks (Eliassen and Palm, 1961; Trenberth, 1986). With 300 hPa in mind, the neighbouring pressure levels in ERA-Interim are 250 and 350 hPa.

To relate the upper-tropospheric EPF-based metric of intraseasonal weather variability to well-known near-surface climatic features such as large-scale circulation indices and time series of regional climate, a number of index time series have been considered for correlation analysis. This pertains to the station-based NAO index based on the pressure difference between Ponta Delgada, Azores, and Reykjavik, Iceland (updated from Jones *et al.*, 1997), available until the end of 2018. Heatwaves and flooding events are supposed to be documented by the self-calibrating Palmer Drought Severity

Index (PDSI) in 5° resolution, averaged over central European land masses in the domain 2.5°E–17.5°N and 42.5°N–57.5°N (available until 2003: Briffa *et al.*, 2009). Finally, time series of monthly 2 m temperature and precipitation have been taken from the gridded Climate Research Unit (CRU) dataset at 0.5° resolution (Harris *et al.*, 2014), averaged over land masses in the same domain as for PDSI. This dataset is currently provided until the end of 2017.

The EPF diagnostics are also applied to a transient climate change projection with the coupled global climate model ECMWF model HAMburg version 5/Max Planck Institute (ECHAM5/MPI-OM) in T63 spectral resolution, equivalent to 1.875° (Jungclaus *et al.*, 2006); in the following, ECHAM5. The simulation is subject to the former high-impact emission scenario A2 (Nakicenovic and Swart, 2000). This model dataset covers the period 1860–2100 and is dedicated to the hypothesis that changes in wave activity and intraseasonal weather variability in the midlatitudes may be affected by global radiative heating (see fourth hypothesis in section 1). ECHAM5 has been widely used in the climatological community (cf. IPCC, 2007) and participates in the Coupled Model Intercomparison Project version 3 (CMIP3) multi-model dataset (Meehl *et al.*, 2007). It has also been found to reproduce the observed leading modes of climate variability at 300 hPa in the North Atlantic region (Delcambre *et al.*, 2013). In addition, Di Biagio *et al.* (2014) have reported that CMIP3 and CMIP5 barely differ in terms of their ability to simulate baroclinic and planetary waves. Note that the choice of the model was not arbitrary; the original intention was to analyse the full multi-model ensemble of CMIP3 and CMIP5 climate change projections in order to assess climate change signals in the EPF diagnostics in a probabilistic sense. However, none of the CMIP3 and CMIP5 data supply centres provides the required climate variables at several higher-tropospheric levels. The ECHAM5 simulation used here could be retrieved from the German CERA (Coupled ECMWF ReAnalysis) database at DKRZ (German Climate Computing Centre) and comprises the 250, 300 and 400 hPa levels.

3 | RESULTS

3.1 | Observed climatological features of EPF diagnostics

As the EPF diagnostics are physically and mathematically complex and related changes more difficult to interpret, the observed climatological structure of the mean circulation and the eddy forcing term are elucidated and explained in this subsection. Figure 1 shows a meridional cross-section of winter and summer temperature, zonal and meridional wind speed between 1,000 and 100 hPa in the North Atlantic study area, averaged over the whole ERA-Interim period. The upper tropospheric frontal zone with temperature being up to 30 °C higher in the subtropics than over the North Pole clearly emerges, especially in winter. In the lower stratosphere above 225 hPa, the temperature gradient is reversed in summer. Zonal wind is characterized by westerlies across the entire sector, except for a small section above the North Pole and in the lower-tropospheric Passat (trade wind) region south of 30°N. In winter, the westerlies peak over the subtropics and mark the position of the subtropical jet stream that arises from the upper-tropospheric branch of the Hadley circulation deflected by the Coriolis force (Szunyogh, 2015). A broad area of strong westerlies extends far into the midlatitudes and stretches down to the 300 hPa level. It is where the polar jet stream (PJ) is located. At the daily time-scale, the PJ is a factor of more than two stronger than the subtropical jet stream. However, it is characterized by high spatio-temporal variability and meandering in a broad belt between 30°N and 60°N. Therefore, it is less apparent from the long-term mean perspective. In boreal summer, the upper-tropospheric westerlies are weaker and the peak area is spatially more confined and shifted polewards. The meridional wind component is one order of magnitude weaker than the zonal wind and most expressed in the upper troposphere and in the subtropical Passat zone. Upper-tropospheric northerlies prevail south of 45°N, while the polar region is marked by upper-tropospheric southerlies. This structure is an expression of the meridional circulation cells, i.e. Ferrel cell and polar cell, which are superimposed on the zonal mean flow (cf. Szunyogh, 2015).

The following analysis focuses on the 300 hPa level because the interaction between mean flow and waves is most present in the upper troposphere and this level lies below the tropopause in all seasons of the year (cf. Trenberth, 1986). As westerlies, cyclogenesis and planetary waves are most active in the cold season (Shepherd, 2016), Northern Hemisphere winter (December–January–February, DJF) is displayed in the following figures. For most maps, a homolographic Lambert projection is chosen, while for wind vector plots an isogonal Mercator projection is more appropriate. The pattern of mean zonal wind velocity at 300 hPa highlights the mean position of the PJ with maximum wind speed of up to 40 $m \cdot s^{-1}$ in the northwest Atlantic and the position of the subtropical jet stream over northern Africa (Figure 2, bottom left). Further downstream over northern Europe westerlies still reach 20 $m \cdot s^{-1}$ in the long-term mean. The meridional wind component is more diversified with southerlies over the northwest Atlantic and over North Africa, in the upper branch of the Hadley circulation (Figure 2, bottom right). In between, northerlies prevail and delineate the range of the Ferrel cell. The resulting vector plot illustrates the areas of maximum westerlies but also a wave-like pattern of the zonal mean flow with an upper-tropospheric trough over eastern North America and a ridge over western Europe (Figure 2, top). This pattern reflects the well-known zonal-wave-number-three structure that emerges in the long-term mean around the

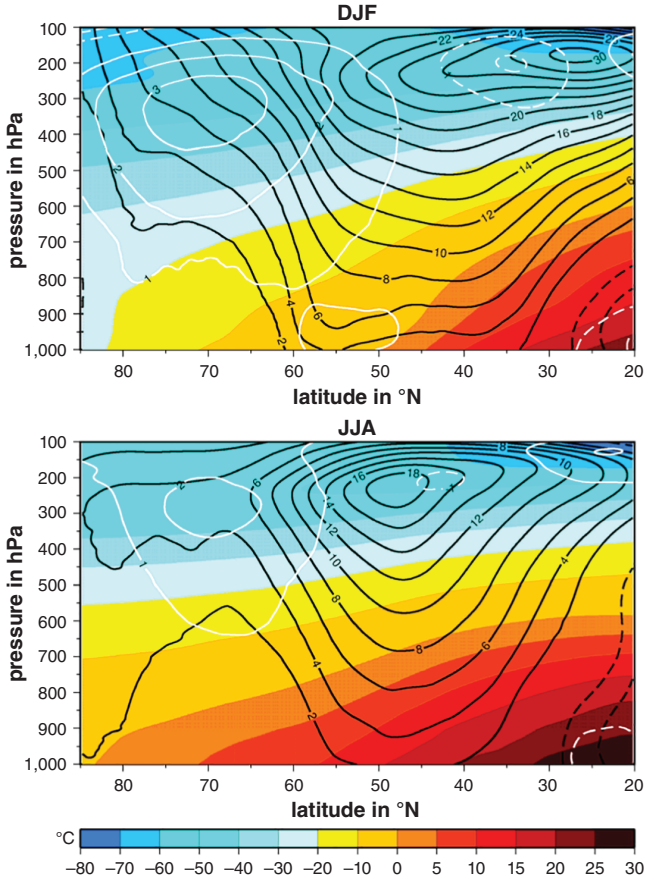

FIGURE 1 Zonal mean of temperature (colour shading), zonal wind (black isolines, m/s) and meridional wind (white isolines, m/s) in DJF (top) and JJA (bottom) in the North Atlantic sector (see domain in Figure 2), ERA-Interim averaged over the 1979–2018 period

Northern Hemisphere due to the topographic impacts of the Rocky Mountains, the Urals and the Tibetan Plateau on the zonal mean flow (Szunyogh, 2015; Paeth *et al.*, 2019). In Northern Hemisphere summer (June–July–August, JJA), the westerlies are noticeably weaker, shifted northwards and confined to a narrower meridional section (not shown).

A first glimpse of atmospheric wave activity associated with the mean flow over the North Atlantic sector is granted by Figure 3. It displays the norm of the zonal EPF vector $\overline{\mathbf{E}_u}$ in Equation 8. which, by the way, is virtually identical to the norm of the meridional EPF vector $\overline{\mathbf{E}_v}$ (compare Equations 8 and 9). In contrast to the divergence of $\overline{\mathbf{E}_u}$, the norm does not indicate the eddy forcing of the mean flow but measures the intensity of macro-turbulence related to atmospheric waves. In the long-term mean, the highest wave activity is found in the vicinity of the subtropical jet stream with its rather fixed position (Figure 3, top). In the midlatitudes, enhanced wave activity is spread over the entire section between 30°N and 50°N, with higher amplitudes over the northwest rather than northeast Atlantic. An important characteristic is given by the fact that the day-to-day variability of wave activity within a season is by a factor of 10 more pronounced than the year-to-year variations of seasonal-mean wave activity (Figure 3, middle and bottom). Therefore, we mainly concentrate on long-term changes in intraseasonal variability of the eddy forcing rather than on long-term trends of mean eddy forcing. As for the mean flow, the situation in JJA exhibits a very similar but spatially more confined pattern with substantially smaller amplitudes (not shown).

The long-term mean of the eddy forcing term in Equations 1 and 2 is mapped in Figure 4. Convergence of the zonal EPF vector usually takes place in the northwest Atlantic, especially in the area south of Greenland (Figure 4, top left). Here, momentum is transferred from the mean flow to atmospheric waves. On the one hand, this pertains to planetary Rossby waves that are stimulated due to orographic forcing over the North American land mass (Shimizu and de Albuquerque Cavalcanti, 2011). On the second hand, it reflects the region of cyclogenesis at the forefront of the upper-tropospheric trough, producing synoptic-scale waves over the northwest Atlantic (Szunyogh, 2015). Divergence of the zonal EPF vector is prevailing further downstream over the eastern Atlantic and Europe. There is a distinct bifurcation with one branch stretching over the Mediterranean Basin, and a second one over the North Sea and Scandinavia. This is in agreement with the major storm tracks and the associated dissipation of wave energy in this sector (Cohen *et al.*, 2014; Szunyogh, 2015). Here, the eddy forcing feeds the kinetic energy of the mean flow against frictional effects over the continent and induces an eastward extension of strong westerlies. In the cyclogenesis region south of Greenland, this pattern is equally governed by synoptic-scale and planetary waves (Figure 4, middle and bottom left). The baroclinic part of the EPF vector plays a clearly more important role than the barotropic part, highlighting the impact of baroclinic instability in midlatitude atmospheric dynamics (not shown).

In terms of the meridional EPF vector (Figure 4, right-hand side), the spatial pattern of convergence and divergence supports the meridional circulation cells with enhanced northerlies south of the PJ (Ferrel cell) and stronger southerlies north of the mean PJ axis (polar cell). At smaller scales, the same takes place near the subtropical jet stream axis over North Africa. Synoptic-scale perturbations and Rossby waves equally contribute to this pattern.

We have also computed the residuum term of the zonal and meridional momentum equations (term VI in Equations 1 and 2) and found out that it is characterized by very small amplitudes, except for some minor effects in the Mediterranean region where the heterogeneous terrain may more perceptibly affect the atmospheric boundary layer (not shown). This implies that the eddy forcing term is indeed the major source of momentum for large-scale atmospheric circulation in the North Atlantic domain. For the summer season, the same

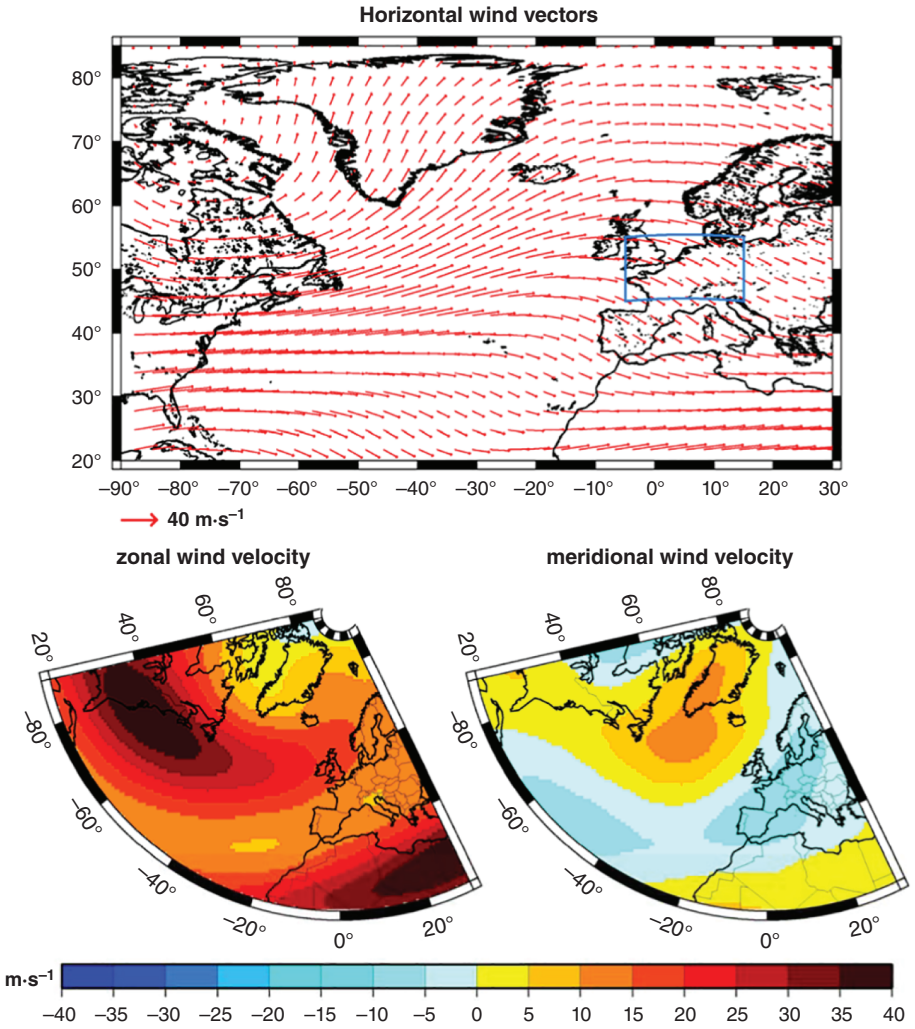

FIGURE 2 Mean horizontal wind vectors (top) and zonal and meridional wind velocity (bottom) in DJF at the 300 hPa level, ERA-Interim averaged over the 1979–2018 period. The blue box in the top figure denotes the central European sector addressed in subsection 3.2

is true for the mean flow and the norm of the EPF vectors: the pattern is more restricted to a narrow band between 40°N and 55°N and the amplitudes are clearly reduced (not shown). Not surprisingly, the interannual and intraseasonal variability of the eddy forcing term is more or less identical to the structure displayed in Figure 3 for the norm of the EPF vectors.

The resulting mean eddy forcing of the horizontal wind vectors is illustrated in Figure 5. The triggering of the meridional circulation cells is most evident, especially in the western North Atlantic. When heat and momentum are exchanged between the mean flow and atmospheric waves, this meridional circulation is crucial to restore the thermal wind balance (Trenberth, 1986; Szunyogh, 2015). At first sight, the distinct northwesterly acceleration of air masses in the northwest Atlantic contradicts the mean flow pattern in Figure 2 (top). Yet, the accelerated air masses are large-scale and subject to the Coriolis force, leading to a gradual eastward deflection and finally feeding the mean westerly flow.

3.2 | Observed changes in EPF diagnostics

In the next step, changes in atmospheric circulation and EPF diagnostics are investigated over the 40-year ERA-Interim data period. This period may be too short (and too early) to capture longer-term transient climate changes due to radiative heating in this highly chaotic system with nonlinear interactions between mean flow, synoptic-scale and planetary waves. Nonetheless, zonal wind velocity exhibits a spatially coherent and statistically significant trend pattern with a distinct northward shift of the PJ axis over the northwest Atlantic and a less pronounced northward shift of the subtropical jet stream over North Africa, whereas westerlies tend to weaken elsewhere (Figure 6, left). This is indicative of a general poleward shift of tropical and extratropical circulation zones and has also been reported for the Southern Hemisphere (e.g. Wilcox *et al.*, 2012; Molnos *et al.*, 2017). It means that over the last 40 years the typical winter situation is getting closer to the former summer situation with the PJ trapped in a more poleward and spatially confined position (see subsection 3.1). Meridional

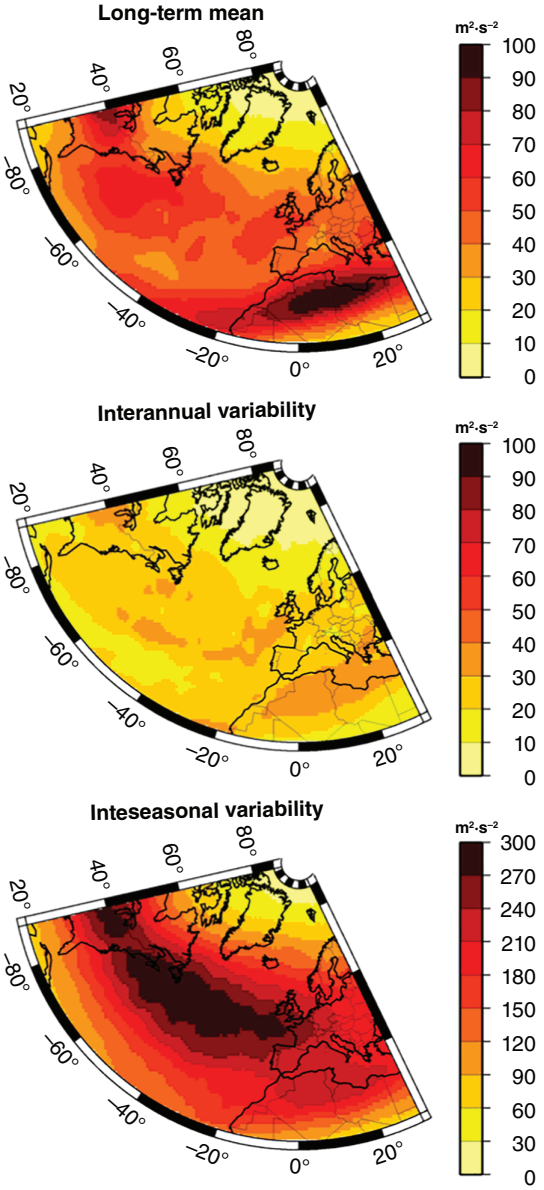

FIGURE 3 Long-term mean (top), interannual standard deviation (middle) and mean intraseasonal standard deviation (bottom) of the norm of the EPF vector (u-component, m^2/s^2) in DJF at the 300 hPa level, ERA-Interim over the 1979–2018 period

wind velocity is less characterized by long-term changes, except for a tendency towards a smaller-scale trough over the western Mediterranean region and a stronger poleward propagation of air masses into the Norwegian Sea (Figure 6, right). In summer, the trend pattern is similar to the one for winter, but the northward shift of the PJ is more distinct over the eastern rather than the western North Atlantic (not shown).

The pattern of changes in the mean eddy forcing term over the last 40 years is less coherent in space and barely significant (hence not shown). It negatively correlates with the mean pattern in Figure 4 (top panels), implying that the exchange of heat and momentum between the mean flow and atmospheric waves tends to decrease slightly, especially with respect to the meridional component. Anyway, the changes in u and v wind components displayed in Figure 6 are not associated with a major change in the mean pattern of the eddy forcing term but to the other terms in Equations 1 and 2 (terms III, IV and/or VI, see section 2). In fact, this finding is not surprising since the mean patterns of the EPF vector divergence illustrated in Figures 4 and 5 are related to the current land–sea distribution and orographic structures that favour a typical Rossby wave pattern over the North Atlantic sector, unaffected at the time-scale of anthropogenic radiative forcing.

As related studies have recently pointed to the decreasing weather variability and increasing persistence of weather anomalies in Northern Hemisphere winter and summer (e.g. de Vries *et al.*, 2013; Vihma, 2014; Perlwitz *et al.*, 2015; Jaiser *et al.*, 2016; Hoffmann, 2018; Pfleiderer and Coumou, 2018), we put particular stress on the intraseasonal variability of the eddy forcing term, hence, on a higher-order statistical moment than the mean. The day-to-day standard deviation of the EPF diagnostics over a season serves as a measure of weather fluctuations related to wave activity. A value of zero, as a hypothetical lower limit, means that there are either no waves, which is unrealistic in the light of omnipresent baroclinic instability within the quasi-stationary wave-number-three-pattern shown in Figure 2, or that the wave pattern does not change within a season. In Figure 7, statistically significant linear changes in DJF intraseasonal variability of the zonal (left) and meridional (right) eddy forcing components are displayed over the 40-year ERA-Interim period. The total changes reveal a distinct poleward shift of intraseasonal weather variability (top panels). This is more striking in the zonal component, whereas the meridional component is more characterized by a widespread decline, especially over Europe and the southeastern United States. Planetary waves make a larger contribution to the general decrease of intraseasonal variability in winter (bottom panels), while synoptic-scale perturbations such as extratropical cyclones perform a systematic northward shift (middle panels). Thus, a detailed look into wave-specific changes is granted by means of the EPF diagnostics.

In Northern Hemisphere summer, the pattern of changing intraseasonal variability is noisier, but most regions are subject to a significant reduction, especially in central Europe (Figure 8, top panels). In particular, this pertains to the sector between 40°N and 60°N where wave activity and eddy forcing peak during summer (see subsection 3.1). Extratropical cyclones are less active in boreal summer and, hence, hardly contribute to the trend pattern (middle panels). In contrast, planetary waves are clearly involved (bottom panels), serving as a potential explanation for more persistent summertime weather across Europe (cf. Horton *et al.*, 2015; Kornhuber *et al.*, 2017; Hoffmann, 2018).

As the upper-tropospheric EPF diagnostics are rather sophisticated and more difficult to interpret in a broader climatological sense, the next step of the analysis is dedicated

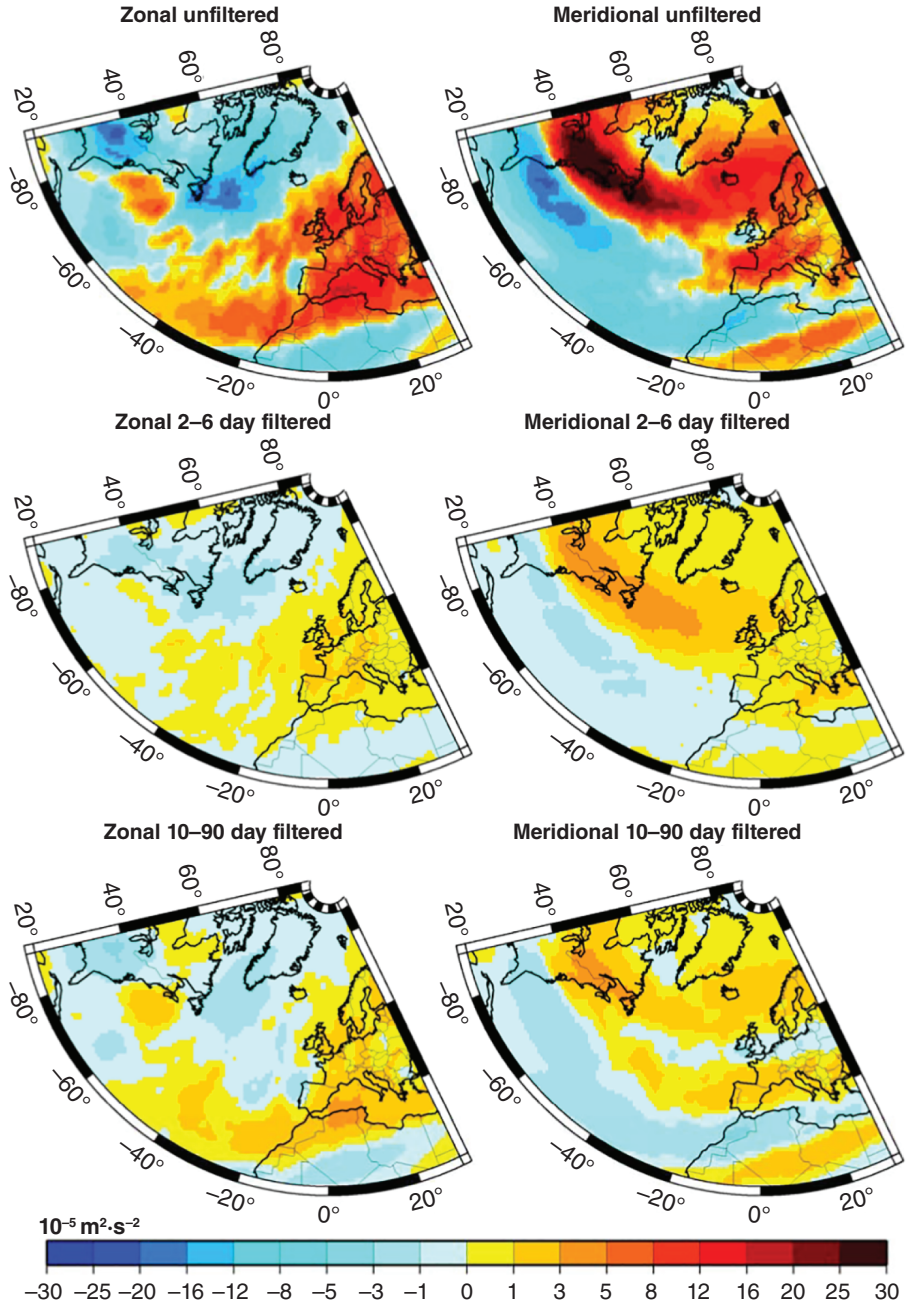

FIGURE 4 Divergence (10^{-5} m/s^2) of EPF vector $\overline{\mathbf{E}_x}$ (left) and $\overline{\mathbf{E}_y}$(right) at 300 hPa for unfiltered daily data (top), 2–6 day filtered data (middle) and 10–90 day filtered data (bottom) in DJF, ERA-Interim averaged over the 1979–2018 period

to the link between the diagnosed changes in intraseasonal weather variability and regional temperature and precipitation anomalies as well as leading teleconnection patterns. For this purpose, seasonal time series of intraseasonal weather variability derived from the EPF diagnostics are built by averaging once over the entire study region (cf. Figure 2) and once over the central European region (5°W–15°E, 45°N–55°N, see subdomain in Figure 2) where observed changes are particularly expressed (cf. Figures 7 and 8). The summer and winter time series for the zonal and meridional EPF components are portrayed in Figure 9. Except for the zonal component in winter, all time series are marked by a statistically significant negative trend (error level of 5%) that is still superimposed on remarkable year-to-year variations. Weather variability and negative trends are more expressed over the European subdomain than over the entire North Atlantic sector. The latter is characterized by larger seasonal differences of wave activity. Obviously, weather variability is more affected further downstream from the major upper-tropospheric trough that is typically located over eastern North America and the northwest Atlantic.

When correlating the time series averaged over central Europe with circulation indices and regional climate indicators, the linear trend has been removed in order to avoid

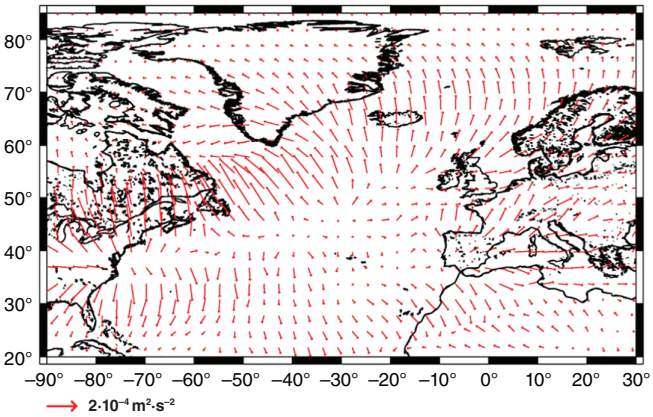

FIGURE 5 Forcing of the horizontal mean flow at 300 hPa by the divergence of EPF vectors $\overline{\mathbf{E}_x}$ and $\overline{\mathbf{E}_y}$ in DJF, ERA-Interim averaged over the 1979–2018 period

statistical relationships that mainly arise from these trend components. The results of the correlation analysis are summarized in Table 1. The first row refers to the NAO index as a major driver of European climate variability, especially in winter (Rauthe and Paeth, 2004; Kim *et al.*, 2014; Vihma, 2014). Indeed, our metric of intraseasonal weather variability during central European winter exhibits positive correlations with the NAO. As to be expected, a strong NAO comes along with enhanced weather variability.

In addition, the time series of intraseasonal variability are linked to regional climate anomalies in central Europe (Table 1, lower three rows). Our metric is a good indicator of temperature anomalies. In winter, the correlation is positive because enhanced wave activity is associated with more cyclones and warm air advection from the North Atlantic to the maritime part of Europe (cf. Rauthe and Paeth, 2004). In summer, the statistical relationship is even stronger but of negative sign, implying that reduced wave activity leads to higher than normal temperatures (cf. Russo *et al.*, 2014; Horton *et al.*, 2015; Coumou *et al.*, 2018). The link to precipitation is also evident but not always statistically significant. In all seasons of the year, the correlation coefficients are positive with more wave activity inducing wetter than normal conditions. A combined index of hydrological drought is given by the PDSI, relying on temperature, precipitation and local parameters for soil and land-surface characteristics (Briffa *et al.*, 2009). Drought is registered as a negative PDSI anomaly. The correlation is weak but partly significant, especially for the zonal EPF component. A positive correlation means that reduced intraseasonal weather variability signifies a tendency towards enhanced drought conditions in central Europe.

3.3 | Simulated changes in EPF diagnostics

In the last step of this analysis, the EPF diagnostics are applied to the transient ECHAM5 experiment with strong radiative forcing. The aim is to evaluate the hypothesis of a potential anthropogenic component in the changing wave activity across the North Atlantic basin (e.g. Mann *et al.*, 2017). Figure 10 displays various characteristics of the atmospheric circulation at 300 hPa as simulated by ECHAM5 during the 1979–2018 period. The patterns can be directly compared with the reanalysis data, displayed in the bottom panels of Figure 2, middle and bottom panels of Figure 3 and top panels of Figure 4. Due to the coarser resolution of the climate model compared with the ERA-Interim reanalysis, the simulated patterns are smoother and exhibit slightly lower amplitudes. However, the basic structure and even various regional details are reproduced in a very reliable way, except for some overestimated westerlies over western Europe and underestimated southerlies over parts of eastern North America. In particular, the split between interannual and intraseasonal variability of the eddy term and the mean patterns of the eddy forcing are in very good agreement between the climate model and the reanalyses. This is a clear indicator that even coarser-grid climate models may be able to assess the observed interactions between mean flow and atmospheric waves in the North Atlantic sector, necessitating a high model skill in terms of all involved atmospheric variables as well as their interplay (see Equations 1–10). This makes the EPF diagnostics a promising tool to study the effects of Arctic amplification on weather variability and extremes in the midlatitudes within a multi-model probabilistic framework.

Figure 11 illustrates the simulated changes of intraseasonal weather variability over the 1979–2100 period that is subject to substantial greenhouse gas increases in the model. In winter (top panels), a strong weakening is projected south of 50°N that is barely compensated by some increases over eastern Canada, eastern Europe, Greenland and the Arctic. The patterns are reminiscent of the observed changes over the last 40 years (Figure 7), but the reduction is spatially more coherent and the poleward shift more obvious. Scaled with the trend period, the simulated changes are less pronounced than the observed ones, as recently suggested by Coumou *et al.* (2018) and Evans *et al.* (2018). In summer (bottom panels), decreasing intraseasonal variability of the eddy forcing is simulated in the entire study region. The changes peak in roughly the same latitudinal belt between 35°N and 55°N as observed (Figure 8). In the climate model, they constitute a physically consistent and spatio-temporally coherent signal of human interference with extratropical atmospheric dynamics, including potential implications for regional climate anomalies and weather extremes. In agreement with the ERA-Interim data (cf. Figures 7 and 8), the simulated total changes in weather variability are more supported by planetary rather than synoptic-scale waves (not shown).

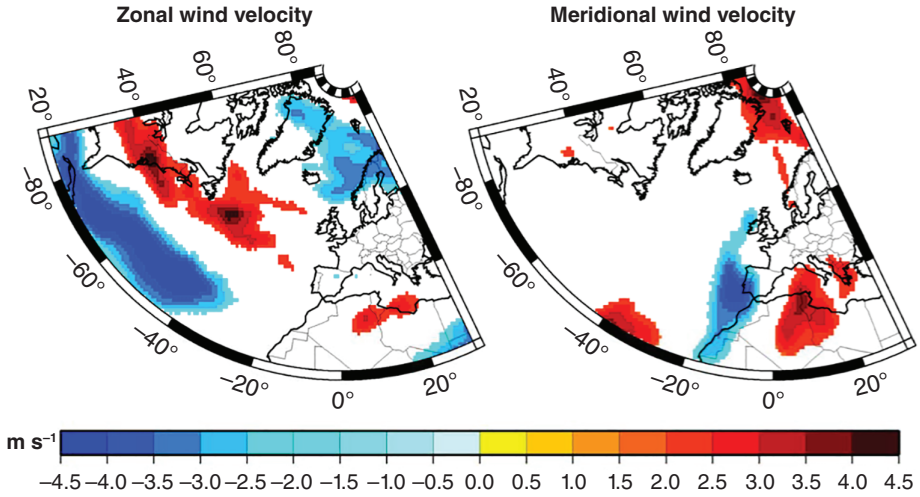

FIGURE 6 Linear changes of zonal (left) and meridional (right) wind velocity (m/s) in DJF at the 300 hPa level, ERA-Interim over the 1979–2018 period. Only changes statistically significant at the 5% level are displayed

TABLE 1 Correlation coefficients between seasonal de-trended time series of intraseasonal variability of the eddy forcing terms at 300 hPa (ERA-Interim averaged over the central European sector, 5°W–15°E, 45°N–55°N) and various climate indices: NAO index, Northern Hemisphere stratospheric aerosol optical depth as well as central European self-calibrating Palmer drought severity index, 2 m temperature and precipitation sums

	***u*-component**				***v*-component**			
	DJF	**MAM**	**JJA**	**SON**	**DJF**	**MAM**	**JJA**	**SON**
NAO	0.61	0.24	−0.24	0.34	0.46	0.45	−0.19	−0.06
PDSI	0.29	0.38	0.28	0.12	−0.12	0.33	0.12	0.08
Temp.	0.31	0.19	−0.57	0.04	0.22	0.39	−0.28	−0.29
Prec.	0.22	0.27	0.31	0.23	0.02	0.13	0.43	0.29

Note: Correlation coefficients statistically significant at the 5% level are marked in red.

4 | DISCUSSION AND CONCLUSIONS

The present study contributes to the issue of changes in midlatitude atmospheric circulation and weather variability. The results and knowledge gained will now be recapped, evaluated with respect to the underlying four scientific hypotheses and discussed in the light of related studies by other authors. The major goal and novel aspect of our investigation is that we close a gap in the physical process chain between a potential weakening and poleward shift of the westerlies in the Northern Hemisphere and the associated response of atmospheric waves. In addition, it is distinguished between synoptic-scale and planetary waves in order to improve our process understanding of the implications of changing wave activity for regional climate and weather extremes. Observed trends are compared with the output of a climate model simulation with strong radiative forcing to support the hypothesis of an anthropogenic trigger.

The issue is exemplified in the North Atlantic sector where adjacent continents have experienced more severe heatwaves and cold spells in recent decades (e.g. Cohen *et al.*, 2014; Coumou *et al.*, 2018) and the density of data to be assimilated in the ERA-Interim reanalysis is relatively high (Dee *et al.*, 2011). To address the interaction between mean flow and atmospheric waves in a physically consistent and mathematically explicit way, the EPF diagnostics are applied. This approach has been successfully used to investigate the impact of shrinking Arctic sea ice and snow cover on midlatitude atmospheric circulation, including the NAO/NAM (Dethloff, 2006; Handorf *et al.*, 2015; Jaiser *et al.*, 2016). We define a new indicator of upper-tropospheric intraseasonal weather variability based on the EPF diagnostics and put it in the context of changing atmospheric dynamics, persistent wave patterns and regional climate anomalies in central Europe, satisfying the call for more sophisticated diagnostics to improve our understanding of dynamical responses to global warming (Nakamura and Zhu, 2010; Huang and Nakamura, 2016; Overland *et al.*, 2016).

The climatological assessment of the observed EPF characteristics can well be explained and interpreted in the light of the mean flow patterns in the upper troposphere

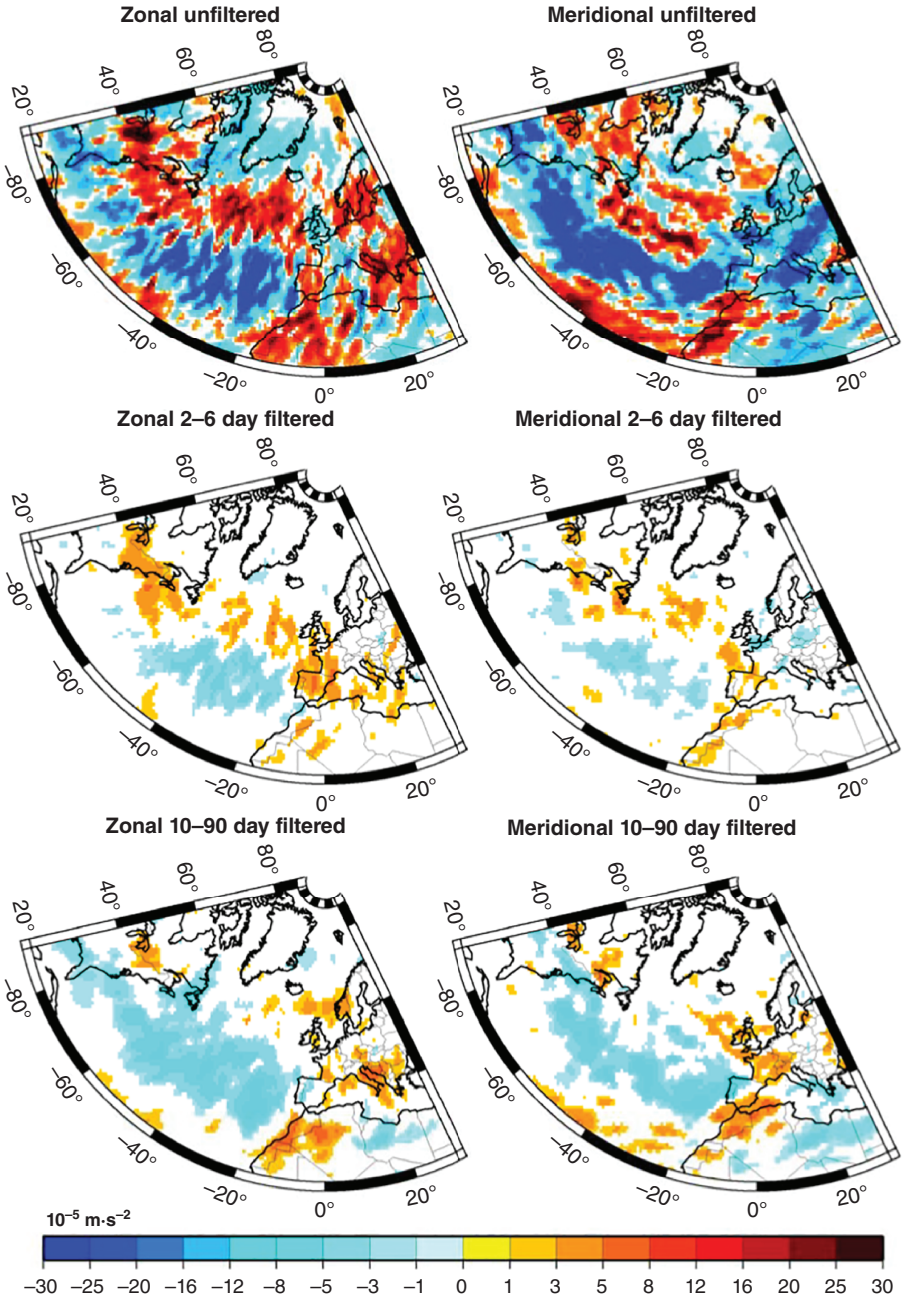

FIGURE 7 Linear changes of intraseasonal weather variability in DJF related to total atmospheric wave dynamics (top), synoptic waves (middle) and planetary waves (bottom) displayed for the divergence of the zonal (left) and meridional (right) EPF vector in DJF at the 300 hPa level, ERA-Interim over the 1979–2018 period. Only changes statistically significant at the 5% level are displayed

and is perfectly in line with theoretical considerations (cf. Szunyogh, 2015): wave activity is highest in the vicinity of the polar and subtropical jet streams, with a much broader latitudinal section occupied by the meandering PJ. At the forefront of the trough-like structure over the northwest Atlantic, convergence of the zonal EPF vector prevails. This means that momentum is transferred from the zonal mean flow to the waves, being in agreement with the stimulation of Rossby waves and cyclogenesis in this area (cf. Shimizu and de Albuquerque Cavalcanti, 2011). Further downstream, the EPF vector is divergent, implying that the eddy forcing supports the zonal mean flow against frictional processes, especially over Europe and the Mediterranean basin. The meridional component of eddy forcing triggers the Ferrel and polar cells and is responsible for the maintenance of the thermal wind balance. Thus, the EPF diagnostics represent a useful process-oriented and interpretable metric to describe the interactions between mean flow and atmospheric waves.

According to our first hypothesis, the EPF approach is able to illustrate observed changes in atmospheric mean

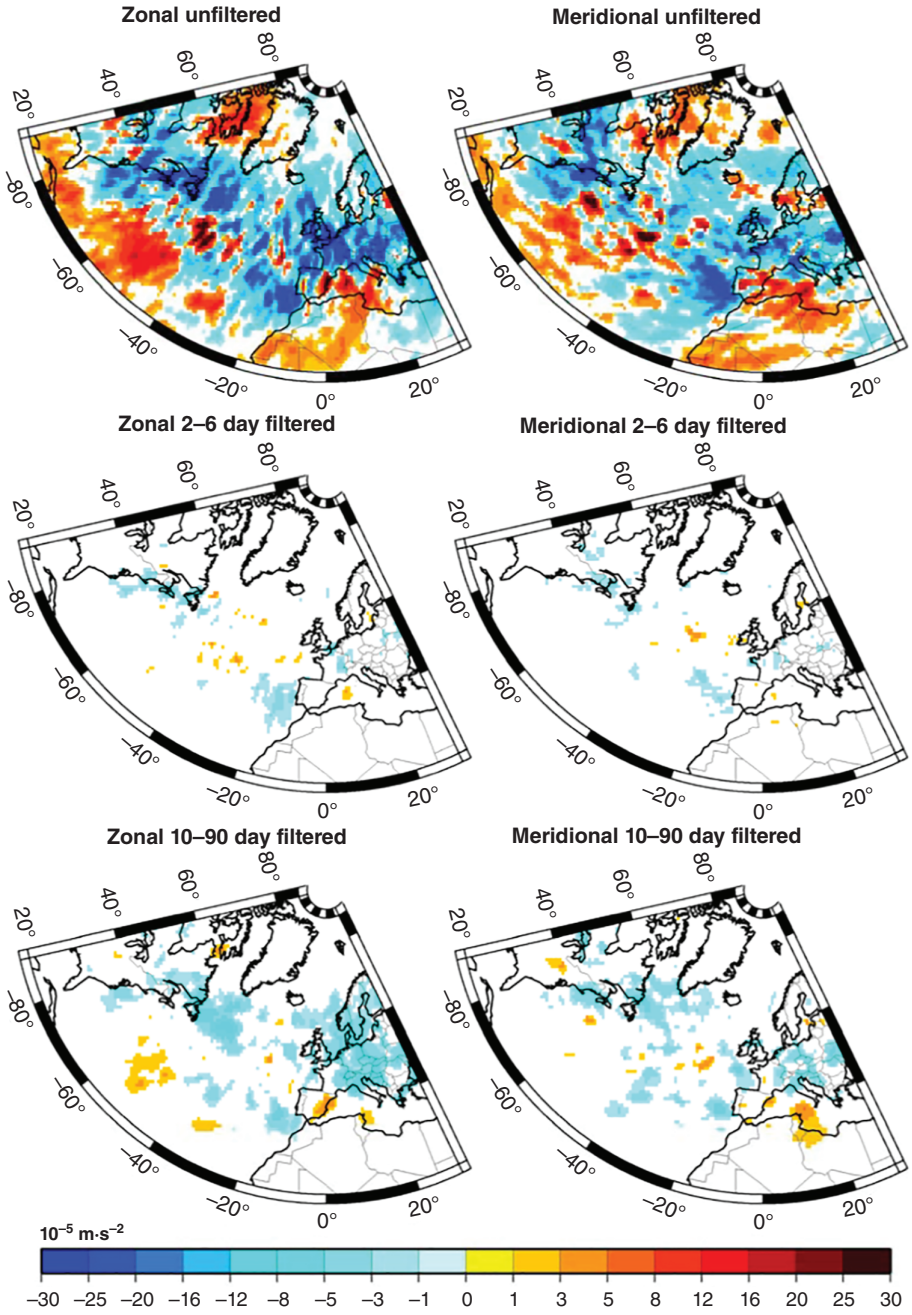

FIGURE 8 Same as Figure 7 but for JJA

flow and wave activity over the last 40 years, especially after 1995 (cf. Cohen *et al.*, 2014). In terms of the mean flow, there is a significant weakening of the westerlies in most parts of the study region and a poleward shift and narrowing of the PJ axis over eastern North America and the North Atlantic. This agrees with the outcome from other work (Wilcox *et al.*, 2012; Molnos *et al.*, 2017). The same is true for the meridional position of the subtropical jet stream over North Africa, indicating that the Tropics are extending poleward, as suggested by Wang (2001), Kossin (2014) and Lucas *et al.* (2014). The meridional wind component is less characterized by long-term changes, except for a stronger wave-like structure over western Europe. De Vries *et al.* (2013) have also pointed to more frequent meridional wave patterns and blocking over Europe.

In winter, intraseasonal weather variability related to atmospheric waves experiences a northward shift and a general weakening over many regions, e.g. central Europe, particularly in the meridional component. The poleward shift is mainly evident in the storm track of extratropical cyclones (cf. McCabe *et al.*, 2001; Mizuta, 2012), whereas planetary waves tend to weaken more widespread. Thus, the physically based EPF diagnostics support the idea of the effect of Arctic amplification on midlatitude weather variability and extremes during winter (Cohen *et al.*, 2014; Vihma, 2014; Perlwitz *et al.*, 2015; Shepherd, 2016). Kim *et al.* (2014)

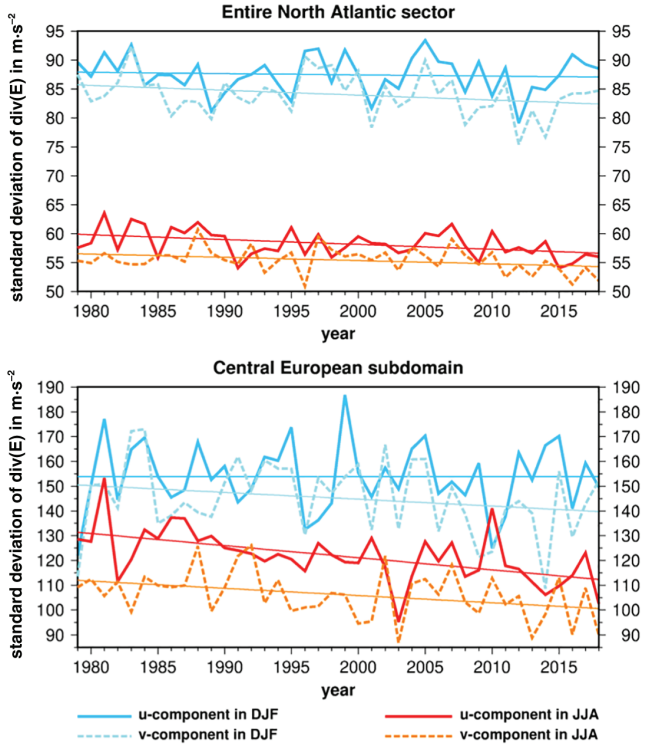

FIGURE 9 Time series of intraseasonal weather variability in DJF and JJA related to total atmospheric wave dynamics displayed for the divergence of the zonal and meridional EPF vector at the 300 hPa level, ERA-Interim averaged over the entire North Atlantic sector (top) and over the central European subdomain (5°W–15°E, 45°N–55°N) (bottom)

have called the more frequently occurring antithetic weather situation with extremely high temperatures over the Arctic and extreme cold surges in the midlatitudes the "warm-Arctic cold-continent pattern".

In summer, decreasing upper-tropospheric intraseasonal weather variability is even more striking, especially across Europe and the North American East Coast. The trend pattern is mainly related to planetary waves that can provoke severer heatwaves in the midlatitudes. In fact, various authors have reported on more frequent and intense heatwaves and dry spells over Northern Hemisphere land masses and relate them to changes in midlatitude atmospheric circulation and persistent wave patterns (Horton *et al.*, 2015; Kornhuber *et al.*, 2017; Coumou *et al.*, 2018; Hoffmann, 2018; Pfleiderer and Coumou, 2018). Obviously, the main effect is reduced cloud cover and enhanced direct solar radiation in anticyclonic weather types (Chang *et al.*, 2016).

At first sight, the assessment of upper-tropospheric intraseasonal weather variability based on the EPF diagnostics is somewhat abstract. However, time series of observed intraseasonal variability in central Europe are linked to large-scale circulation indices such as the NAO and to regional near-surface temperature and precipitation anomalies. The correlation coefficients agree with what is expected from the known relationships between large-scale teleconnection patterns, atmospheric wave activity and regional climate in terms of the NAO (cf. Vihma, 2014; Handorf *et al.*, 2015). This makes our approach interpretable in a broader climatological framework.

The second hypothesis suggests that the upper-tropospheric atmospheric features and processes diagnosed by the EPF approach can be reproduced by coarse-grid global climate models. This is an advantage when it comes to the assessment of anthropogenic climate change signals in a multi-model ensemble framework. The direct comparison of observed and simulated mean flow and EPF characteristics reveals an excellent agreement, even with respect to many regional details. Delcambre *et al.* (2013) have pointed out that CMIP3 models generally reproduce the observed leading modes of variability at the 300 hPa level and de Vries *et al.* (2013) found a high agreement in terms of blocking situations between this particular ECHAM5 model and reanalysis data. Nonetheless, we were positively surprised by the model performance with respect to the eddy forcing and its interannual and intraseasonal variability because other authors have demonstrated that low-resolution global climate models exhibit remarkable deficiencies in the simulation of atmospheric dynamics, especially in a multivariate setting (e.g. Berckmans *et al.*, 2013; Steinhaeuser and Tsonis, 2014). Indeed, the EPF diagnostics require such a multivariate setting (see section 2). Unfortunately, the high model skill of ECHAM5 cannot be generalized due to the lack of available upper-tropospheric data from other global climate models in the CMIP3 and CMIP5 framework. Therefore, there is only limited support for the second hypothesis.

The third hypothesis addresses the assessment of changes in intraseasonal variability in the context of anthropogenic climate change. The considered climate model projection with high-impact emission scenario predicts a general weakening of day-to-day weather variability in summer across the entire North Atlantic sector. In winter, a distinct poleward shift prevails. It is not surprising that man-made radiative forcing plays a crucial role in the analysed process chain since the Arctic amplification as a potential origin of the whole process chain is closely related to melting sea ice and reduced snow cover. Several authors have revealed an anthropogenic component in changing extratropical wave patterns and persistence (e.g. Russo *et al.*, 2014; Paeth *et al.*, 2015; Mann *et al.*, 2017), partly involving anthropogenic forcing by aerosols (Rotstayn *et al.*, 2014). The more striking finding is that the long-term changes foreshadowed by the transient model run are similar to the ones observed in the recent past, at least regarding the basic patterns. A closer look manifests that the amplitude of observed changes is larger than the simulated response as highlighted before by Chang *et al.* (2016) and Evans *et al.* (2018). In summary, there is substantiated

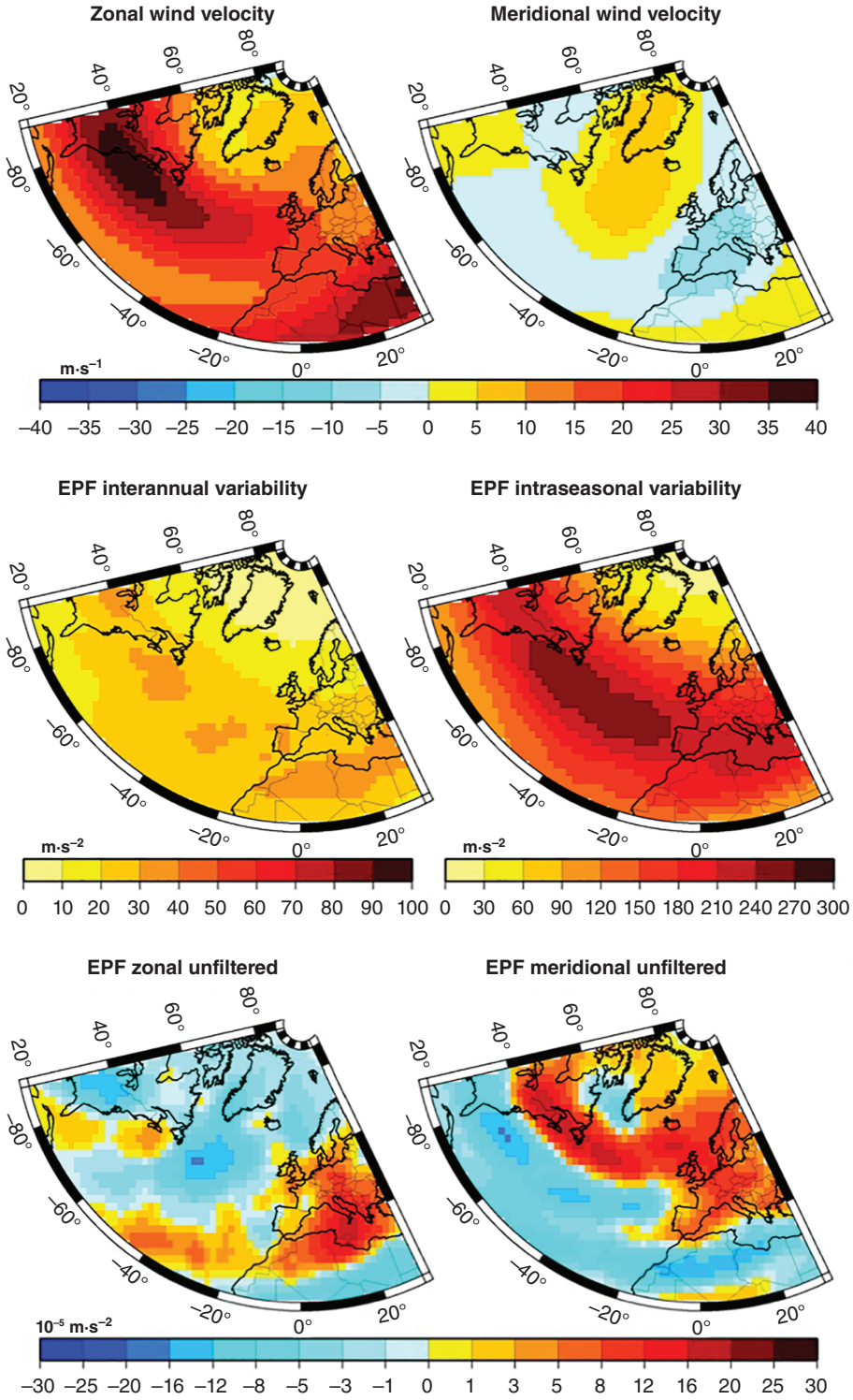

FIGURE 10 Mean horizontal wind vectors (top panels), interannual standard deviation and mean intraseasonal standard deviation of the norm of vector $\overline{E_x}$ (middle panels), divergence of EPF vector ($\overline{\mathbf{E}_x}$) and ($\overline{\mathbf{E}_y}$) (bottom panels) for unfiltered daily data in DJF in 300 hPa, ECHAM5 averaged over the 1979–2018 period

evidence in favour of the third hypothesis from climate model data and potentially also from reanalyses.

One limitation of our analysis is that only one global climate change simulation with the required upper-tropospheric pressure levels was available. Therefore, we were unable to detect a climate change signal in the sense of state-of-the-art probabilistic climate prediction (cf. IPCC, 2013). In the next step, the EPF diagnostics must be applied to a multi-model ensemble of climate model simulations. As it is unlikely that the necessary model data can still be retrieved for

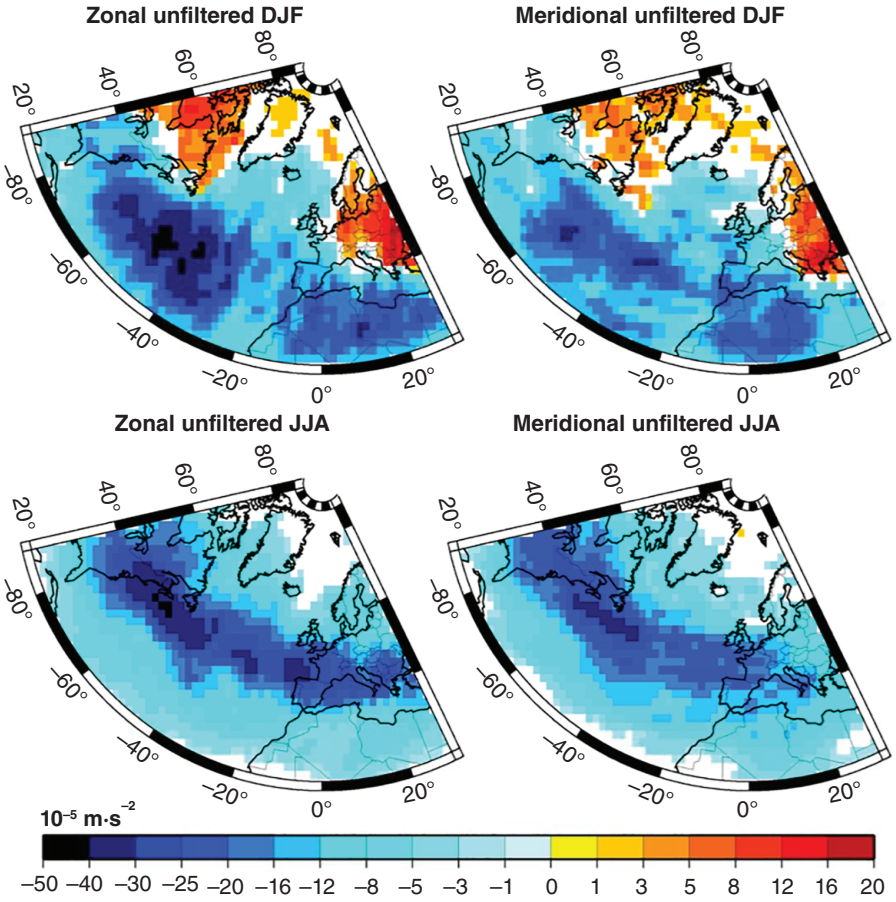

FIGURE 11 Linear changes of intraseasonal weather variability in DJF (top) and JJA (bottom) related to total atmospheric wave dynamics displayed for the divergence of the zonal (left) and meridional (right) EPF vector at the 300 hPa level, ECHAM5 over the 1979–2100 period. Only changes statistically significant at the 5% level are displayed

the whole of CMIP3 and CMIP5 models, we plead for an improved availability of upper-tropospheric data in the upcoming CMIP6 environment.

Another open question is how the process chain suggested here fits into the prevalence of positive NAO and NAM trends in most climate model projections (e.g. Paeth and Pollinger, 2010), whereas the present study and other authors (e.g. Vihma, 2014; Handorf *et al.*, 2015) have shown that reduced westerlies and more persistent wave patterns are associated with negative NAO phases. More research is required to assess whether and how both processes can occur within the same dataset (cf. Shepherd, 2014; Overland *et al.*, 2016). In fact, there is still a lack of process understanding concerning the impact of radiative heating on changes in midlatitude atmospheric dynamics. An interesting approach would be to compute the diabatic heating sources over the Atlantic under changing oceanic and atmospheric circulation. As recent observations since the year 2000 do not support the tendency towards a positive NAO as predicted by many models, it is an important matter of future investigation to compare NAO trends and changes in intraseasonal weather variability in the next-generation CMIP6 climate models.

ACKNOWLEDGEMENTS

We thank the ECMWF for providing the ERA-Interim reanalyses, the Climatic Research Unit for delivering the updated PDSI, the NAO index and the gridded temperature and precipitation data, the Max-Planck climate modeler group for producing and the DKRZ for making the ECHAM5/MPI-OM model data available. We are grateful to Andreas Hense for helpful discussions and two anonymous reviewers for their very valuable comments and suggestions.

ORCID

Heiko Paeth https://orcid.org/0000-0001-8145-4706

REFERENCES

Barnes, E.A. and Screen, J.A. (2015) The impact of Arctic warming on the midlatitude jet-stream: can it? Has it? Will it? *WIREs Climate Change*, 6, 277–286.

Berckmans, J., Woollings, T., Demory, M.E., Vidale, P.-L. and Roberts, M. (2013) Atmospheric blocking in a high-resolution climate model: influences of mean state, orography and eddy forcing. *Atmospheric Science Letters*, 14, 34–40.

Blackmon, M.L. (1976) A climatological spectral study of the 500 mb geopotential height of the Northern Hemisphere. *Journal of the Atmospheric Sciences*, 33, 1607–1623.

Briffa, K.R., van der Schlier, G. and Jones, P.D. (2009) Wet and dry summers in Europe since 1750: evidence of increasing drought. *International Journal of Climatology*, 29, 1894–1905.

Chang, E.K.M., Ma, C., Zheng, C. and Yau, A.M.W. (2016) Observed and projected decrease in Northern Hemisphere extratropical cyclone activity in summer and its impacts on maximum temperature. *Geophysical Research Letters*, 43, 2200–2208.

Cohen, J., Screen, J.A., Furtado, J.C., Barlow, M., Whittleston, D., Coumou, D., Francis, J., Dethloff, K., Entekhabi, D., Overland, J. and Jones, J. (2014) Recent Arctic amplification and extreme mid-latitude weather. *Nature Geoscience*, 7, 627–637.

Coumou, D., Di Capua, G., Vavrus, S., Wang, L. and Wang, S. (2018) The influence of Arctic amplification on mid-latitude summer circulation. *Nature Communications*, 9, 2959. https://doi.org/10.1038/s41467-018-05256-8.

Dee, D.P., Uppala, S., Simmons, A., Berrisford, P., Poli, P., Kobayashi, S., Andrae, U., Alonso-Balmaseda, M., Balsamo, G., Bauer, P., Bechtold, P., Beljaars, A., van de Berg, L., Bidlot, J.-R., Bormann, N., Delsol, C., Dragani, R., Fuentes, M., Geer, A.J., Haimberger, L., Healy, S., Hersbach, H., Hólm, E.V., Isaksen, L., Kållberg, P.W., Köhler, M., Matricardi, M., McNally, A., Monge-Sanz, B.M., Morcrette, J.-J., Peubey, C., de Rosnay, P., Tavolato, C., Thépaut, J.-N. and Vitart, F. (2011) The ERA-interim reanalysis: configuration and performance of the data assimilation system. *Quarterly Journal of the Royal Meteorological Society*, 137, 553–597.

Delcambre, S.C., Lorenz, D.J., Vimont, D.J. and Martin, J.E. (2013) Diagnosing Northern Hemisphere jet portrayal in 17 CMIP3 global climate models: twentieth-century intermodal variability. *Journal of Climate*, 26, 4910–4929.

Dethloff, K., Rinke, A., Benkel, A., Køltzow, M., Sokolova, E., Saha, S.K., Handorf, D., Dorn, W., Rockel, B., von Storch, H., Haugen, J.E., Røed, L.P., Roeckner, E., Christensen, J.H. and Stendel, M. (2006) A dynamical link between the Arctic and the global climate system. *Geophysical Research Letters*, 33(3), L03703. https://doi.org/10.1029/2005GL025245.

Di Biagio, V., Calmanti, S., Dell'Aquila, A. and Ruti, P.M. (2014) Northern Hemisphere winter midlatitude atmospheric variability in CMIP5 models. *Geophysical Research Letters*, 41, 1277–1282.

Eliassen, A. and Palm, E. (1961) On the transfer of energy in stationary mountain waves. *Geofysiske Publikasjoner*, 22, 1–23.

Evans, D., Sagoo, N., Renema, W., Cotton, L.J., Müller, W., Todd, J.A., Kumar Saraswati, P., Stassen, P., Ziegler, M., Pearson, P.N., Valdes, P.J. and Affek, H.P. (2018) Eocene greenhouse climate revealed by coupled clumped isotope-Mg/Ca thermometry. *Proceedings of the National Academy of Sciences*, 115, 1174–1179.

Handorf, D., Jaiser, R., Dethloff, K., Rinke, A. and Cohen, J. (2015) Impacts of Arctic sea ice and continental snow cover changes on atmospheric winter teleconnections. *Geophysical Research Letters*, 42, 2367–2377.

Harris, I., Jones, P.D., Oborn, T.J. and Lister, D.H. (2014) Updated high-resolution grids of monthly climatic observations – the CRU TS3.10 dataset. *International Journal of Climatology*, 34, 623–642.

Hoffmann, P. (2018) Enhanced seasonal predictability of the summer mean temperature in central Europe caused by new dominant weather patterns. *Climate Dynamics*, 50, 2799–2812.

Horton, D.E., Johnson, N.C., Singh, D., Swain, D.L., Rajaratnam, B. and Diffenbaugh, N.S. (2015) Contribution of changes in atmospheric circulation patterns to extreme temperature trends. *Nature*, 522, 465–469.

Huang, C.S. and Nakamura, N. (2016) Local finite-amplitude wave activity as a diagnostic of anomalous weather events. *Journal of the Atmospheric Sciences*, 73, 211–229.

IPCC. (2007) *Climate Change 2007, the Physical Science Basis, Working Group I Contribution to the Fourth Assessment Report of the Intergovernmental Panel on Climate Change*. Cambridge, UK: Cambridge University Press.

IPCC. (2013) *Climate Change 2013, the Physical Science Basis, Working Group I Contribution to the Fifth Assessment Report of the Intergovernmental Panel on Climate Change*. Cambridge, UK: Cambridge University Press.

Jaiser, R., Nakamura, T., Handorf, D., Dethloff, K., Ukita, J. and Yamazaki, K. (2016) Atmospheric winter response to Arctic Sea ice changes in reanalysis data and model simulations. *Journal of Geophysical Research: Atmospheres*, 121, 7564–7577.

Jones, P.D., Jónsson, T. and Wheeler, D. (1997) Extension to the North Atlantic Oscillation using early instrumental pressure observations from Gibraltar and south-west Iceland. *International Journal of Climatology*, 17, 1433–1450.

Jungclaus, J.H., Keenlyside, N., Botzet, M., Haak, H., Öuo, J.J., Latif, M., Marotzke, J., Mikolajewicz, U. and Roeckner, E. (2006) Ocean circulation and tropical variability in the coupled model ECHAM5/MPI-OM. *Journal of Climate*, 19, 3952–3972.

Kim, B.-M., Son, S.-W., Min, S.-K., Jeong, J.-H., Kim, S.-J., Zhang, X., Shim, T. and Yoon, J.-H. (2014) Weakening of the stratospheric polar vortex by Arctic sea-ice loss. *Nature Communications*, 5, 4646.

Kornhuber, K., Petoukhov, V., Petri, S., Rahmstorf, S. and Coumou, D. (2017) Evidence for wave resonance as a key mechanism for generating high-amplitude quasi-stationary waves in boreal summer. *Climate Dynamics*, 49, 1961–1979.

Kossin, J.P. (2014) The poleward migration of the location of tropical cyclone maximum intensity. *Nature*, 509, 349–352.

Lucas, C., Timbal, B. and Nguyen, H. (2014) The expanding Tropics: a critical assessment of the observational and modeling studies. *Wiley Interdisciplinary Reviews: Climate Change*, 5, 89–112.

Mann, M.E., Rahmstorf, S., Kornhuber, K., Steinman, B.A., Miller, S.K. and Coumou, D. (2017) Influence of anthropogenic climate change on planetary wave resonance and extreme weather events. *Scientific Reports*, 7, 45242.

McCabe, G.J., Clark, M.P. and Serreze, M.C. (2001) Trends in Northern Hemisphere surface cyclone frequency and intensity. *Journal of Climate*, 14, 2763–2768.

Meehl, G.A., Covey, C., Taylor, K.E., Delworth, T., Stouffer, R.B.M.J., Latif, M., McAvaney, B. and Mitchell, J.F. (2007) The WCRP CMIP3 multimodel dataset: a new era in climate change research. *Bulletin of the American Meteorological Society*, 94, 21–25.

Mizuta, R. (2012) Intensification of extratropical cyclones associated with the polar jet change in the CMIP5 global warming projections. *Geophysical Research Letters*, 39(19), L19707. https://doi.org/10.1029/2012GL053032.

Molnos, S., Mamdouh, T., Petri, S., Nocke, T., Weinkauf, T. and Coumou, D. (2017) A network-based detection scheme of the jet stream core. *Earth System Dynamics*, 8, 75–89.

Nakamura, N. and Solomon, A. (2010) Finite-amplitude wave activity and mean flow adjustments in the atmospheric general circulation. Part I: Quasigeostrophic theory and analysis. *Journal of the Atmospheric Sciences*, 67, 3967–3983.

Nakamura, N. and Solomon, A. (2011) Finite-amplitude wave activity and mean flow adjustments in the atmospheric general circulation. Part II: Analysis in the isentropic coordinate. *Journal of the Atmospheric Sciences*, 68, 2783–2799.

Nakamura, N. and Zhu, D. (2010) Finite-amplitude wave activity and diffusive flux of potential vorticity in eddy–mean flow interaction. *Journal of the Atmospheric Sciences*, 67, 2701–2716.

Nakicenovic, N. and Swart, R. (2000) *Emissions Scenarios, 2000, Special Report of the Intergovernmental Panel on Climate Change*. Cambridge, UK: Cambridge University Press.

Overland, J.E., Dethloff, K., Francis, J.A., Hall, R.J., Hanna, E., Kim, S.-J., Screen, J.A., Shepherd, T.G. and Vihma, T. (2016) Nonlinear response of mid-latitude weather to the changing Arctic. *Nature Climate Change*, 6, 992–999.

Paeth, H., Müller, M. and Mannig, B. (2015) Global versus local effects on climate change in Asia. *Climate Dynamics*, 45, 2151–2164.

Paeth, H. and Pollinger, F. (2010) Enhanced evidence for changes in extratropical atmospheric circulation. *Tellus*, 62A, 647–660.

Paeth, H., Steger, C., Li, J., Pollinger, F., Mutz, S.G. and Ehlers, T.A. (2019) Comparison of climate change from Cenozoic surface uplift and glacial–interglacial episodes in the Himalaya–Tibet region: insights from a regional climate model and proxy data. *Global and Planetary Change*, 177, 10–26.

Perlwitz, J., Hoerling, M. and Dole, R. (2015) Arctic tropospheric warming: causes and linkages to lower latitudes. *Journal of Climate*, 28, 2154–2167.

Petoukhov, V., Petri, S., Kornhuber, K., Thonicke, K., Coumou, D. and Schellnhuber, H.-J. (2018) Alberta wildfire 2016: apt contribution from anomalous planetary wave dynamics. *Nature Scientific Report*, 8, 12375. https://doi.org/10.1038/s41598-018-30812-z.

Pfleiderer, P. and Coumou, D. (2018) Quantification of temperature persistence over the Northern Hemisphere land-area. *Climate Dynamics*, 51, 627–637.

Rauthe, M. and Paeth, H. (2004) Relative importance of Northern Hemisphere circulation modes in predicting regional climate change. *Journal of Climate*, 17, 4180–4189.

Rotstayn, L.D., Plymin, E.L., Collier, M.A., Boucher, O., Dufresne, J.-L., Luo, J.-J., von Salzen, K., Jeffrey, S.J., Foujols, M.-A., Ming, Y. and Horowitz, L.W. (2014) Declining aerosols in CMIP5 projections: effects on atmospheric temperature structure and midlatitude jets. *Journal of Climate*, 27, 6960–6977.

Russo, S., Dosio, A., Graversen, R.G., Sillmann, J., Carrao, H., Dunbar, M.B., Singleton, A., Montagna, P., Barbola, P. and Vogt, J.V. (2014) Magnitude of extreme heat waves in present climate and their projection in a warming world. *Journal of Geophysical Research: Atmospheres*, 119, 12500–12512.

Shepherd, T.G. (2014) Atmospheric circulation as a source of uncertainty in climate change projections. *Nature Geoscience*, 7, 703–708.

Shepherd, T.G. (2016) Effects of a warming Arctic. *Science*, 353, 989–990.

Shimizu, M.H. and de Albuquerque Cavalcanti, I.F. (2011) Variability patterns of Rossby wave source. *Climate Dynamics*, 37, 441–454.

Steinhaeuser, K. and Tsonis, A.A. (2014) A climate model intercomparison at the dynamics level. *Climate Dynamics*, 42, 1665–1670.

Szunyogh, I. (2015) *Applicable Atmospheric Dynamics: Techniques for the exploration of atmospheric dynamics*. Singapore: World Scientific Publishing.

Trenberth, K.E. (1986) An assessment of the impact of transient eddies on the zonal mean flow during a blocking episode using localized Eliassen–Palm flux diagnostics. *Journal of the Atmospheric Sciences*, 43, 2070–2087.

Vihma, T. (2014) Effects of Arctic Sea ice decline on weather and climate: a review. *Surveys in Geophysics*, 35, 1175–1214.

de Vries, H., Woollings, T., Anstey, J., Haarsma, R.J. and Hazeleger, W. (2013) Atmospheric blocking and its relation to jet changes in a future climate. *Climate Dynamics*, 41, 2643–2654.

Wang, C. (2001) Atlantic climate variability and its associated atmospheric circulation cells. *Journal of Climate*, 15, 1516–1536.

Wilcox, L.J., Charlton-Perez, A.J. and Gray, L.J. (2012) Trends in Austral jet position in ensembles of high- and low-top CMIP5 models. *Journal of Geophysical Research*, 117, D13115. https://doi.org/10.1029/2012JD017597.

Wilks, D.S. (2006) *Statistical Methods in the Atmospheric Sciences*. Amsterdam: Academic Press.

How to cite this article: Paeth H, Pollinger F. Changes in mean flow and atmospheric wave activity in the North Atlantic sector. *Q J R Meteorol Soc*. 2019;145:3801–3818. https://doi.org/10.1002/qj.3660